journal of the mechanical behavior of biomedical materials 125 (2022) 104945

Contents lists available at ScienceDirect

Journal of the Mechanical Behavior of Biomedical Materials

journal homepage: www.elsevier.com/locate/jmbbm

Research Paper

On the corrosion, stress corrosion and cytocompatibility performances of ALD TiO_2 and ZrO_2 coated magnesium alloys

M. Peron [a,*], R. Bertolini [b], S. Cogo [c,d]

[a] Department of Industrial and Mechanical Engineering, Norwegian University of Science and Technology, Richard Birkelands vei 2b, 7034, Trondheim, Norway
[b] Department of Industrial Engineering, University of Padova, Via Venezia 1, 35131, Padova, Italy
[c] School of Biological Sciences, Health and Life Sciences Building, University of Reading, Whiteknights, RG6 6EX, Reading, United Kingdom
[d] Department of Biology, University of Padova, Via Ugo Bassi 58/b, 35131, Padova, Italy

ARTICLE INFO

Keywords:
Magnesium alloys
Atomic layer deposition (ALD)
Coatings
Stress corrosion cracking (SCC)
Cytotoxicity
Corrosion

ABSTRACT

Magnesium alloys are increasingly studied as materials for temporary implants. However, their high corrosion rate and susceptibility to corrosion-assisted cracking phenomena, such as stress corrosion cracking (SCC), continue to prevent their mainstream use. Recently, coatings have been considered to provide an effective solution to these issues and researchers have focused their attention on Atomic Layer Deposition (ALD). ALD stands out as a coating technology due to the outstanding film conformality and density achievable, and has shown encouraging preliminary results in terms of reduced corrosion rate and reduced SCC susceptibility. Here, we contribute to the ongoing interest in ALD-coated Mg alloys, providing a comprehensive characterisation of the effect of 100 nm thick ALD TiO_2 and ZrO_2 coatings on the corrosion behaviour and SCC susceptibility of AZ31 alloy. Moreover, we also investigate the effect of these coatings on the induced biological response. Our results suggest that the ALD coatings can improve the corrosion and SCC resistance of the Mg alloy, with the ZrO_2 ALD coating showing the best improvements. We suggest that the different corrosion behaviours are the cause of the cytocompatibility results (only the ZrO_2 ALD coating was found to meet the demands for cellular applications). Finally, we leverage on considerations about the coatings' wettability, electrochemical stability and surface integrity to justify the different results.

1. Introduction

The number of persons undergoing surgical operations involving the insertion of medical devices has been steadily increasing in recent years, particularly orthopaedic surgery (Ginebra et al., 2006). Injuries may require replacement implants, in extreme trauma cases, or temporary fixation devices (namely bone plates, screws, rods, or intramedullary nails), to temporarily sustain the bone during the healing period (Peron et al., 2020a).

Stainless steel, cobalt-chromium based alloys, titanium and titanium-based alloys are widely used for such orthopaedic applications, owing to their chemical inertness in the human body and high impact strength and wear resistance (Hanawa, 2010). Nevertheless, their high elastic moduli may lead to stress-shielding phenomena. This would make the regenerated bone weaker at the implant site since the applied force mostly transmits through the implant rather than on the newly formed bone (Bauer and Schils, 1999; Salahshoor and Guo, 2012). This may cause the implant to loosen, leading to subsequent fracture (Salahshoor and Guo, 2012). Besides, after the new tissue has grown back, the implant must be surgically removed. This is associated with an increased risk of infection as well as an additional burden to the health-care system (Pound, 2014).

Polymers and ceramics, which are biodegradable, are being studied extensively to overcome these disadvantages (Peron et al., 2017). However, their adoption as temporary devices in load bearing applications is still limited because of the poor stiffness and brittleness that characterises polymers and ceramics, respectively.

Magnesium-based alloys have been suggested as an ideal candidate biomaterial for temporary devices because of their low elastic modulus and biodegradability. Actually, the release of Mg^{2+} ions during in vivo corrosion would not only be safe for the patient but it could also help with new bone formation and strengthen the bone-implant interface, since magnesium acts as an enzymatic cofactor (Hänzi et al., 2009).

Despite the advantages offered by magnesium as a biomaterial, its

* Corresponding author.
E-mail address: mirco.peron@ntnu.no (M. Peron).

https://doi.org/10.1016/j.jmbbm.2021.104945
Received 6 August 2021; Received in revised form 23 October 2021; Accepted 26 October 2021
Available online 30 October 2021
1751-6161/© 2021 The Authors. Published by Elsevier Ltd. This is an open access article under the CC BY license (http://creativecommons.org/licenses/by/4.0/).

application is limited for two reasons: (i) the poor corrosion resistance of magnesium alloys may cause the implant to lose mechanical strength before the bone healing process is complete (Song, 2007) and (ii) alloying elements, like aluminium (Al) and rare-earths, commonly used to alligate magnesium for improving its corrosion resistance, are not suitable to be used in the human body.

For this reason, many techniques have been proposed to increase the corrosion resistance of magnesium alloys, such as cryogenic machining, severe plastic deformation techniques like equal channel angular pressing, and surface coating treatments (Peron et al., 2020b, 2020c). Among the latter, Atomic Layer Deposition (ALD) has attracted great interest among researchers and practitioners due to its potential. Indeed, ALD is a new nanofabrication and surface engineering technology based on successive, self-limiting, and self-saturating surface chemical reactions that lead to highly controlled and conformal coatings, even on high-aspect ratio structures.

Compared to other approaches, ALD is applicable to non-uniform and non-planar surfaces and it allows a precise thickness control of the coating, leading to improved corrosion resistance (Peron et al., 2020d). In addition, it requires a low deposition temperature, thus avoiding any kind of microstructural modification of the magnesium substrate, and promoting the formation of a hard and adherent coating (Kania et al., 2021). Many attempts have been made to evaluate whether ALD is suitable to guarantee Mg alloy surface protection from corrosive media environments for biomedical purposes.

In (Kania et al., 2021), thin films of two different thicknesses of titanium dioxide (TiO_2) were deposited onto a $MgCa_2Zn_1Gd_3$ alloy by means of the ALD method. Electrochemical tests and hydrogen evolution volume showed reduced corrosion rates compared to the uncoated alloy. In addition, it was reported that the thicker the coating, the higher the corrosion resistance. In (Yang et al., 2017) a compact zirconia (ZrO_2) nanofilm was created on the surface of a magnesium-strontium alloy by ALD method. It was demonstrated that, by adjusting the thickness of the nanofilm, it was possible to modulate the corrosion rate of Mg–Sr alloy, meeting the different requirements of the clinical devices. In (Marin et al., 2012a), three different ALD coatings (including TiO_2, alumina (Al_2O_3) and a combination of them) were deposited on AZ31 magnesium alloy substrates. Polarisation curves showed that ALD deposition can be successfully used to protect AZ31 magnesium alloy against corrosion in saline solution. Specifically, multi-layered structures proved to be more effective against corrosion than single layer coatings, being able to reduce the impedance modulus by three orders of magnitude, compared to the substrate alone.

The literature review suggests that ALD represents an efficient way to protect magnesium against corrosion. However, other aspects must be considered, like stress corrosion cracking, (the resistance of the implant when a load is applied under a corrosion environment), as well as cytocompatibility (the interaction between the coating surface and cells). Encouraging results addressing these questions were previously published by the authors (Peron et al., 2020d, 2021), nevertheless, a comprehensive investigation is needed.

Therefore, the present work aims to fulfil this gap, presenting a complete study on corrosion performance and in vitro degradation of TiO_2 and ZrO_2 ALD-coated magnesium alloy. To do this, we carried out an extensive corrosion campaign, with both static and mechanical assisted corrosion approach. The former was evaluated in terms of potentiodynamic polarisation curves and hydrogen evolution tests while, the latter, in terms of slow strain rate tests. All corrosion tests were performed in a simulated body fluid solution at 37 °C, with the aim of being as close as possible to human body conditions. In addition, fracture surfaces were analysed by means of Scanning Electron Microscopy (SEM) to provide insights on the failure mechanisms. Finally, the cytocompatibility was evaluated by measuring the cell viability over time.

Results show that ALD coating on magnesium alloy can provide a suitable way to overcome its corrosion susceptibility. In addition, ZrO_2 represents the best choice as a biomedical coating due to its higher corrosion performance and cytocompatibility.

2. Material and methods

2.1. Material

Commercially available AZ31 magnesium alloy bars of 12 mm diameter and 2000 mm length were purchased from Dynamic Metals Ltd (Leighton Buzzard, UK). The AZ31 magnesium alloy chemical composition and mechanical properties are given in Table 1 and Table 2, respectively.

For the microstructural investigation, discs were cut from the bar, cold-mounted and polished according to the standard procedures. Then, samples were etched by using a solution of alcohol (95 ml), picric acid (5 g), and acetic acid (10 ml) for 10 s. Finally, samples were inspected by using a Leica DMRE™ optical microscope (Leica Microsystems, Wetzlar, Germany) equipped with a high-definition digital camera. The grain size was measured using the linear intercept method. The microstructures along the section of the as-received bar are shown in Fig. 1, revealing a homogeneous matrix with an average grain size of 13.2 ± 8 μm.

2.2. ALD coating deposition and characterisation

A commercial ALD reactor (Savannah S200, Veeco Instruments Inc., Massachusetts, USA) was used for depositing ALD coatings on magnesium surfaces. Two different types of coating (ZrO_2 and TiO_2) were successfully deposited by means of a two-step process.

For ZrO_2, Tetrakis (dimethylamino) zirconium (TDMAZ) and deionized water (H_2O) were made to react at 160 °C to obtain a 100 nm thick coating.

The first step consisted of a 250-ms TDMAZ precursor pulse and a 10 s high purity N_2 purge (semiconductor grade) with a flow rate of 20 sccm, to remove residual reactants and by-products from the chamber and separate the chemical vapour deposition reactions. Afterwards, the second part consisted of a 150 ms H_2O precursor pulse and a 15 ms high purity N_2 purge. The ZrO_2 deposition rate was approximately 1.08 Å/cycle.

With respect to TiO_2, the metal organic precursor used was the Tetrakis (dimethylamido) titanium (IV) (TDMA-Ti), which was heated to 75 °C. The first cycle step consisted of a pulse of a 0.1 s TDMA-Ti precursor and purge of 5 s high-purity N_2 purge with a flow rate of 20 sccm, while the second step consisted of a pulse of 0.015 s H_2O precursor and a purge of 5 s high-purity N_2 purge. The deposition rate was equal to 0.5 Å/cycle.

The chemical composition of the ALD deposited coatings (TiO_2 and ZrO_2) was determined through X-ray photoelectron spectroscopy (XPS). Specifically, the measurements were carried out on TiO_2 and ZrO_2 thin films deposited on p-doped <100> 500 μm thick, 2 inch Si wafers, in order to have a minimum effect of the underlying substrate. Before carrying out the chemical characterisation, the surface was etched for 3 min at an energy of 2 KeV to remove any effects from environmental contamination or surface oxidation.

2.3. Coating adhesion

The adhesion of the TiO_2 and ZrO_2 coatings was evaluated by means of pull-off adhesion test. The pull-off adhesion tests were carried out according to ASTM D 4541 using a pull-off tester (PosiTest AT from DeFelsko). The tests were carried out on 2 mm thick, 60 mm long and 25

Table 1
Chemical composition (wt%) of AZ31 magnesium alloy.

Element	Al	Zn	Mn	Si	Fe	Ca	Mg
wt (%)	3.1	0.73	0.25	0.02	0.005	0.0014	Balance

Table 2
Physical and mechanical properties of AZ31 magnesium alloy.

Density (g/cm^3)	Yield strength (MPa)	Tensile strength (MPa)	Elongation (%)
1.78	150–220	256.3 ± 8.7	24.5 ± 0.7

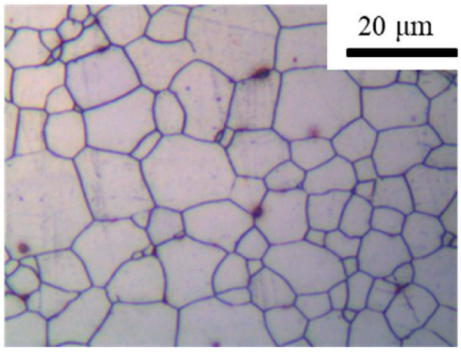

Fig. 1. AZ31 alloy microstructure.

mm wide plates, which were manufactured from the bars, grounded with 2000 SiC paper, and then washed with distilled water and acetone before coating them according to Section 2.2. To carry out the tests, we used dollies with a diameter of 14 mm, which were glued to the surface of the coated samples using a cyano-acrylate adhesive. The tests were carried out at a strain rate equal to 1 MPa/s until failure (either of the adhesive or of the coating). For each coating material, four tests were carried out. Moreover, to determine the glues strength, dollies were glued also on bare samples.

2.4. Corrosion assessment of ALD samples

The electrochemical behaviour of ALD-coated samples was studied using a standard three electrode cell, where the AZ31 bare or coated samples were the working electrode, a Hg/Hg_2SO_4 the reference electrode, and a platinum plate the counter electrode. For this purpose, the magnesium samples (working electrodes) were machined from the bar into discs, characterised by a thickness of 2 mm and a diameter of 29 mm. Afterwards, they were ground with 2000 SiC paper, then washed with distilled water and acetone. Finally, the samples were coated according to Section 2.2 and mounted on cold setting resin. One single specimen surface, with an area of approximately 1 cm^2, was exposed to the corrosive solution.

A Gamry Reference 600+ potentiostat was used for the electrochemical tests. The potentiodynamic polarisation curves were obtained, applying a potential from −3 V to −1 V at a scan rate of 0.5 mVs^{-1}. The potentiodynamic polarisation curves were obtained through testing in Simulated Body Fluid (SBF) solution, prepared according to (Kokubo and Takadama, 2006), at 37 ± 1 °C, in order to closely reproduce the human body conditions.

The corrosion potential (Ecorr) and the corrosion current density (icorr) were determined from the polarisation measurements using the Tafel extrapolation method, according to the ASTM G5-14 standard (ASTM G5, 2019). The corrosion curves were calculated three times in order to assure the results reproducibility.

Evolved hydrogen gas measurements were subsequently performed, in order to acquire additional information on the corrosion rate of coated samples. Importantly, magnesium alloys display a peculiar electrochemical behaviour, the so-called Negative Difference Effect (NDE), that is substantially different from that typical of most metals (Curioni, 2014). Due to the NDE, the estimation of the corrosion rate based solely on a polarisation curve is incomplete, because the NDE greatly distorts the normal polarisation curve. For this reason, hydrogen gas measurement represents a useful additional tool to assess corrosion behaviour of coated samples.

When placed in aqueous solution, magnesium reacts according to Eq (1):

$$Mg + H_2O = Mg^{2+}\ 2OH^- + H_2 \quad (1)$$

For each magnesium atom that dissolves, one molecule of hydrogen gas is produced. In other words, determining the volume of hydrogen that has evolved is equivalent to assessing the weight that has been lost (Song et al., 2013).

First, samples were cut into cubic specimens of 5 mm each side, ground with 2000 grit silicon carbide paper and coated as described in Section 2.2. Then, coated samples were exposed to SBF solution, prepared according to (Kokubo and Takadama, 2006).

Fig. 2 shows a schematic representation of the experimental apparatus designed for the evolved hydrogen gas measurements. The hydrogen produced by the machined sample was collected by a funnel located just above the sample, and then into a burette, placed over the funnel. The amount of evolved hydrogen was determined by measuring the displacement of the solution level in the burette. All of the test equipment was placed in a climatic chamber that assured a constant temperature of 37 ± 1 °C for 7 days.

2.5. Slow strain rate tests (SSRT)

Slow Strain Rate Tests (SSRT) were performed on a 50 kN MTS E45 hydraulic machine equipped with a custom-made chamber to create the corrosion environment.

The experimental setup, schematised in Fig. 3, is mainly composed of: (1) a corrosion chamber equipped with channels for corrosion solution inlet (2) and outlet (3), (4) a submersible pump for continuous circulation of the fluid through the corrosion chamber and (5) a heating element to set the temperature at 37 °C, immersed in a water bath (6). The specimen (7) was grabbed on the hydraulic grips of the machine (8).

Specimens were manufactured by turning the as-delivered bar to a final dog-bone shape with gauge dimensions of 20 mm (length) and 6 mm (diameter), in accordance to ASTM E466 standard (ASTM International and ASTM-E466-96, 1520). The dog bone samples were then ground with 2000 grit SiC paper and, subsequently, cleaned with ethanol and de-ionized water prior to coating.

SSRT tests were carried out at a fixed strain rate of $3.5 \cdot 10^{-6}$ s^{-1} in SBF solution held at human body temperature. The strain rate value was chosen in accordance to the literature, to make magnesium alloys susceptible to SSRT (Padekar et al., 2013).

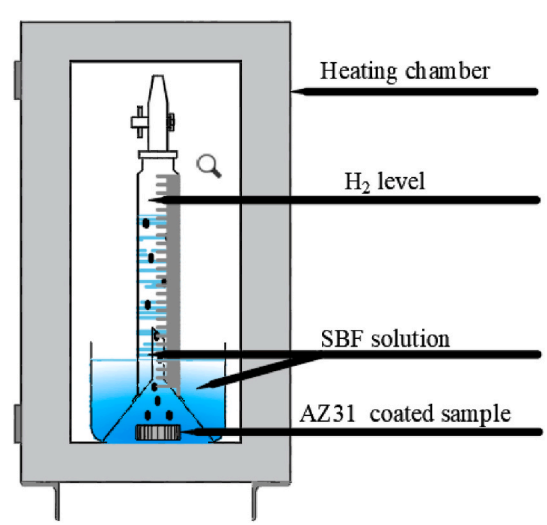

Fig. 2. Scheme of the evolved hydrogen gas measurement setup.

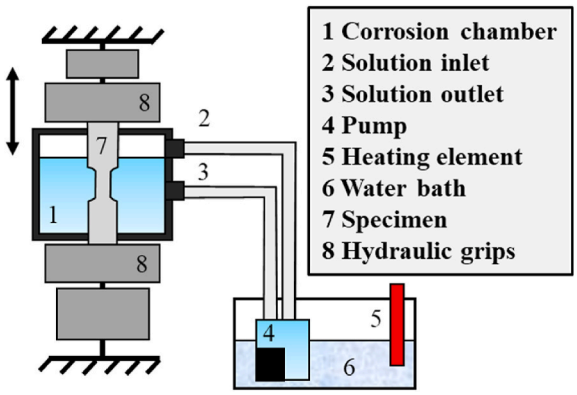

Fig. 3. Scheme of the evolved SSRT setup.

The susceptibility indices I_{UTS} and I_{ε} were calculated according to Eq. (2) and Eq. (3), respectively:

$$I_{SCC} = \frac{UTS_{air} - UTS_{SBF}}{UTS_{air}} \tag{2}$$

$$I_{\varepsilon} = \frac{\varepsilon_{air} - \varepsilon_{SBF}}{\varepsilon_{air}} \tag{3}$$

where UTS is the Ultimate Tensile Strength and ε is the elongation at failure, both evaluated during tests conducted in SBF and air.

The higher the values of I_{SCC}, I_{ε} the greater the SSRT susceptibility, whereas I_{SCC}, I_{ε} tending to zero suggests immunity to SSRT (Choudhary et al., 2014).

2.6. Fractography

The specimen fracture surfaces after SSRTs were cleaned by immersion for 1 min in a solution prepared using 50 g chromium trioxide (CrO_3), 2.5 g silver nitrate ($AgNO_3$) and 5 g barium nitrate ($Ba(NO_3)_2$) in 250 ml distilled water, as suggested in (Thirumalaikumarasamy et al., 2014). The specimens were then washed with distilled water and, finally, ultrasonically cleaned in acetone for 10 min. The fracture surfaces were observed by means of a FEI™ QUANTA 450 SEM (Thermo Fisher Scientific Inc., USA).

2.7. Cell culture studies

Cytotoxicity studies were previously described (Peron et al., 2020b). Briefly, L929 murine fibroblasts were cultured in complete Dulbecco's Modified Eagle Medium (DMEM), supplemented with 10%v/v fetal bovine serum (FBS), 100 U/ml penicillin and 100 μg/ml streptomycin. Extracts were prepared by incubating coated and bare samples in complete DMEM with 1.25 ml/cm^2 extraction ratio for 72 h at 37 °C, in a humidified atmosphere with 5% CO2 (ISO 10993-12:2012, 1099; ISO 10993-5:2009, 1099). After collection and centrifugation of the supernatants, 100% extracts were employed for the cell proliferation assay. 3 × 10^3 L929 cells/wells were seeded on 96-well plates and incubated for 24 h to allow attachment. Starting on the following day, 100 μl of the different extracts were added to each well after 1, 3 and 5 days of treatment, with complete DMEM acting as a negative control. Subsequently, cytotoxicity was assessed via the MTS cell proliferation assay (Promega). The generation of coloured formazan by reduction of the MTS tetrazolium compound was monitored by measuring absorbance at 490 nm on a VICTOR™X3 plate reader (PerkinElmer, Massachusetts, USA).

3. Results

3.1. ALD film characterisation

The chemical composition of the ALD deposited TiO_2 coating was evaluated by carrying out high resolution regional scans for oxygen, titanium and carbon. The regional scans of oxygen and titanium are reported in Fig. 4a and b, respectively. The amount of carbon detected was instead negligible, indicating an ideal deposition process in light of the absence of any contamination. As shown in Fig. 4a, oxygen is present in the form of oxygen atoms in the TiO_2 phase, which leads to the peak at 531 eV (Yu et al., 2000), and in hydroxyl groups, present in the form of impurities (responsible for the small shoulder at higher energy). The regional scan of titanium (Fig. 4b), then, reveals that Ti is present in the Ti^{4+} oxidation state in TiO_2 (Nezar et al., 2017). This is indicated by the peaks corresponding to the core level binding energies of Ti $2p_{3/2}$ and Ti $2p_{1/2}$ (i.e. 459 eV and 464 eV, respectively). Moreover, Ti is present in the form of Ti^{3+} due to the argon etching step, as indicated by the shoulder at lower energy around 456 eV (Kim et al., 1999). With respect to the composition, we observed an oxygen deficient deposition. We found in fact 60% oxygen and 40% titanium, while the expected stochiometric composition is Ti and oxygen in the ratio 1:2 (i.e. 66.7% oxygen and 33.3% titanium). The quantification calculation was carried out using CASAXPS software.

Dealing with the ALD deposited ZrO_2 coating, then, the chemical composition was evaluated by means of high-resolution regional scans for oxygen, zirconium and carbon. As for the TiO_2 coating, a nearly carbon-free ALD deposition was confirmed by the lack of peaks in the high-resolution scan for the element carbon. The high-resolution spectra for oxygen and zirconium are reported in Fig. 5a and b, respectively. The former revealed that oxygen is present in form of ZrO_2 (this is deducible from the peak at 530 eV) and ZrO (the oxidation of metal in air leads to the shoulder on the higher energy side), while the latter showed two peaks at binding energy 182 eV and 184 eV, which correspond to Zr $3d_{5/2}$ and Zr $3d_{3/2}$, respectively. As for the case of TiO2 coating, a thin film of oxygen-deficient zirconia was revealed by the quantification calculation using CASAXPS software (the composition was 40% Zr and 60% O).

Furthermore, the thickness of the deposited coatings was determined using spectroscopic ellipsometry. A fixed angle of incidence of 65° was used. Specifically, the measurements were carried out on Si wafers coated in the same deposition process as the Mg substrates. The results reported the thickness of the TiO_2 and ZrO_2 coatings to be 100.98 and 100.97 nm, respectively.

Finally, SEM analyses were used to evaluate the presence of cracks on the TiO_2 and ZrO_2 coated samples. Representative images are reported in Fig. 6(a–d), together with images the one representative of the surface state after grinding (e, f), for sake of comparison. It can be appreciated that cracks located in the substrate appear wider and longer compared to those on coating. Therefore, cracks present on the coating can be attributed to the different coefficient of thermal expansion between substrate and coating (please refer to the "Discussion" section for more details) and not to the manufacturing step performed before coating.

Moreover, Table 3 reports the average crack density and length.

Table 3 shows that the average crack density and length decreased moving from TiO_2 to ZrO_2 coated samples.

3.2. Coating adhesion

Table 4 reports the results of the pull-off adhesion tests for both coated materials.

The pull-off adhesion tests for both coating materials are characterized by glue failures. Results reported in Table 4 witness that both TiO_2 and ZrO_2 coatings are characterized by strong adhesion, since it exceeds the one of the glue (the glue strength was found to be 24.8 ± 3.65. MPa).

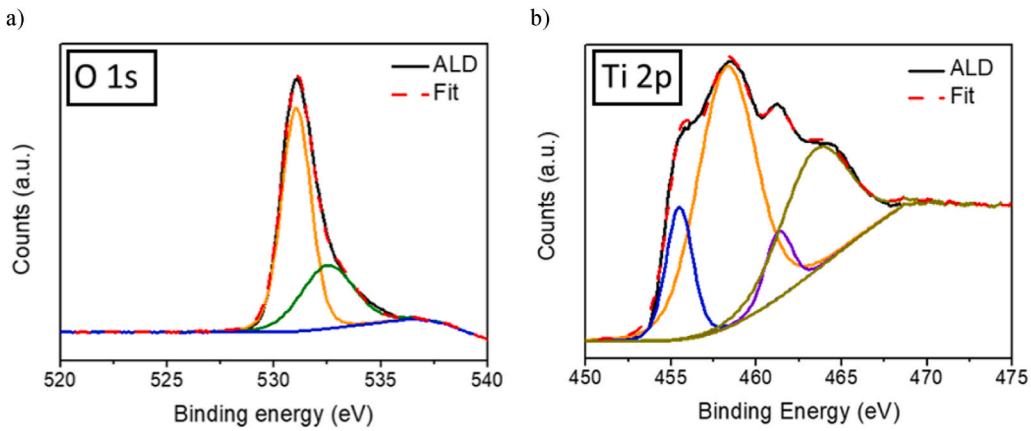

Fig. 4. XPS spectra for ALD deposited TiO_2. The regional scan of O 1s (a) shows that oxygen is present in the form of oxygen atoms in the TiO_2 phase (see peak at 531 eV) and of hydroxyl groups in impurities (see the small shoulder at higher energy). The regional scan of Ti 2p (b) shows that Ti is present in the Ti^{4+} oxidation state in TiO_2 (see the peaks at 459 eV and 464 eV corresponding to the core level binding energies of Ti $2p_{3/2}$ and Ti $2p_{1/2}$, respectively). Moreover, Ti is present in the form of Ti^{3+} due to the argon etching step (see shoulder at around 456 eV).

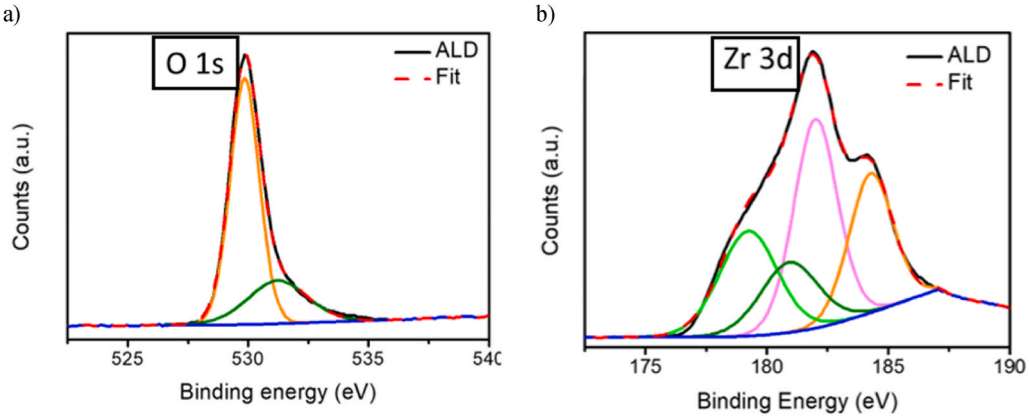

Fig. 5. XPS spectra for ALD deposited ZrO_2. The regional scan of O 1s (a) shows that oxygen is present in the form of ZrO_2 (see peak at 530 eV) and ZrO (see the shoulder on the higher energy side). The regional scan for Zr 3d (b) shows that Zr is present as ZrO_2 (see peaks at binding energy 182 eV and 184 eV, corresponding to the core level binding energies of Zr $3d_{5/2}$ and Zr $3d_{3/2}$).

3.3. Corrosion resistance of ALD samples

Fig. 7 shows the potentiodynamic polarisation curves of the ALD TiO_2 and ZrO_2 coated samples as compared to the bare sample. The results show that the corrosion resistance of the Mg samples is higher in the presence of the coating. In fact, the lower the corrosion current density, the higher the corrosion resistance. This is consistent with previous reports (Yang et al., 2017; Liu et al., 2011, 2018), which link the increased corrosion resistance of coated samples to their barrier properties (Peron et al., 2020d; Huang et al., 2019). Moreover, it can also be seen that ALD ZrO_2 coatings result in a more effective protection than ALD TiO_2 coatings, in agreement with previous results (Peron et al., 2020e, 2021). This statement is further clarified in Table 5, where the average values of the corrosion current densities are reported together with the average values of the corrosion potentials.

3.4. Hydrogen evolution tests

The results of the hydrogen evolution experiments are reported in Fig. 8.

The results of the hydrogen evolution tests agree with those of the potentiodynamic polarisation tests, suggesting that the application of coatings can limit the corrosion of AZ31 alloy. Moreover, as previously found in Section 3.2, the ALD ZrO_2 coating provides a better protection than the ALD TiO_2 counterpart: although TiO_2 is able to reduce the hydrogen evolved from the bare sample by 52%, in the presence of ZrO_2 hydrogen evolution is reduced by up to 93%.

Finally, it is interesting to observe the behaviour of the bare samples: after an initial phase where it increases rapidly, the hydrogen evolution rate significantly decreases. This can be explained by considering the corrosion products present on the surface. At first, in fact, the bare alloy is covered by a surface layer of MgO and/or $Mg(OH)_2$ that forms spontaneously. This surface layer, however, is responsible for the high corrosion rate since it is very soluble in a water environment. The continuation of the corrosion process, then, leads to an increase in the pH of the surroundings. This, in turn, causes the precipitation of Ca-phosphate on the surface, which is protective, hence determining the reduction of the observable corrosion rate (Esmaily et al., 2017).

3.5. SSRT behaviour of ALD samples

The results of the slow strain rate tests in SBF are reported in Fig. 9, where the results related to the samples tested in an inert environment (air) are also reported for the sake of comprehension. Specifically, the engineering stress-strain curve for the bare samples are reported in Fig. 9a, while those for ALD TiO_2 and ZrO_2 coated samples are reported in Fig. 9b and c, respectively. Moreover, the results of the slow strain rate tests are compared in Fig. 10 in terms of Ultimate Tensile Strength (UTS) and elongation at failure.

As widely reported (Peron et al., 2020b, 2020c, 2020e), the surface modification did not influence the tensile properties of the samples when tested in air: the strength and ductility of the bare samples are comparable with those of the ALD coated samples. However, when tested in SBF, the ALD TiO_2 and ZrO_2 coated samples showed a considerably higher elongation to failure than the bare counterparts. This indicates a lower susceptibility of the coated samples to the SCC

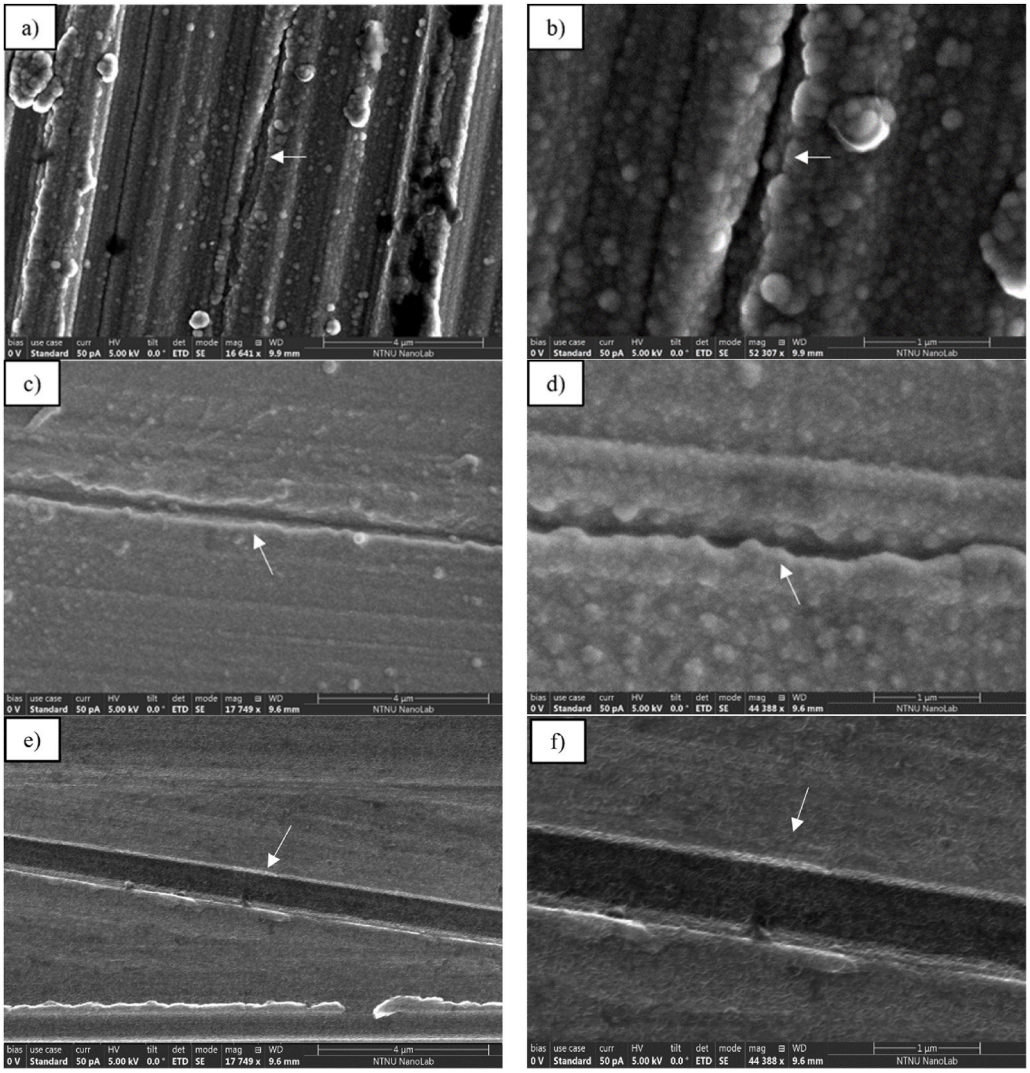

Fig. 6. Representative SEM images of cracks formed on TiO_2 coated (a and b), ZrO_2 coated discs (c and d) and substrate (e and f). The cracks are highlighted by the white arrows.

Table 3
Average crack length and density (meant as number of cracks per square cm) detected for the different coatings.

	TiO_2	ZrO_2
Crack density (n° cracks/cm^2)	0.87 ± 0.37	0.61 ± 0.28
Average Crack length (μm)	4.54 ± 3.05	3.14 ± 2.41

Table 4
Adhesion strengths obtained for the different coatings.

	TiO_2	ZrO_2
Adhesion strength (MPa)	24.52 ± 4.04	25.15 ± 3.26

phenomenon (as indicated by the SCC indexes reported in Fig. 10). From the results it can be seen that ALD ZrO_2 coatings were the most effective in reducing the SCC susceptibility; the elongation to failure of the bare samples tested in SBF was, in fact, increased by 223%, while with ALD TiO_2 coatings by 'just' 126%.

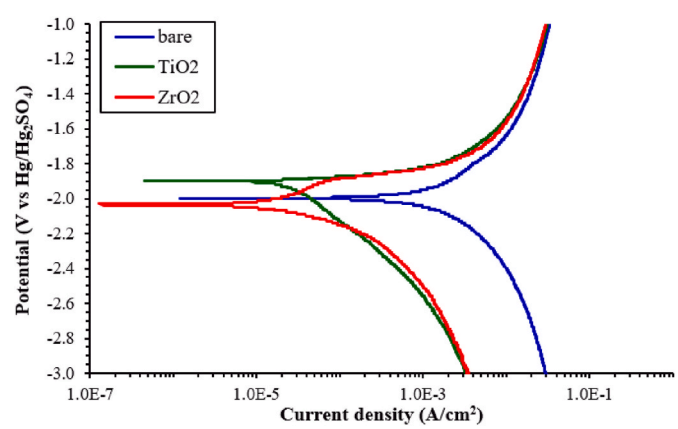

Fig. 7. Potentiodynamic polarisation curves of bare, ALD TiO_2 and ZrO_2 coated AZ31 alloy in SBF.

3.6. Fracture surfaces

Fracture surfaces of the bare samples tested in SBF are reported in Fig. 11a and b. The overall view of the fracture surface shows mixed

Table 5
Corrosion potentials (E_{corr}) and corrosion current densities (i_{corr}) for bare and coated AZ31 samples in SBF.

	Bare	TiO_2 coating	ZrO_2 coating
E_{corr} (V)	−2.00 ± 0.02	−1.90 ± 0.01	−2.02 ± 0.01
I_{corr} (A/cm^2)	3.0 10^{-3} ± 0.4	2.5 10^{-5} ± 0.6	1.2 10^{-6} ± 0.3

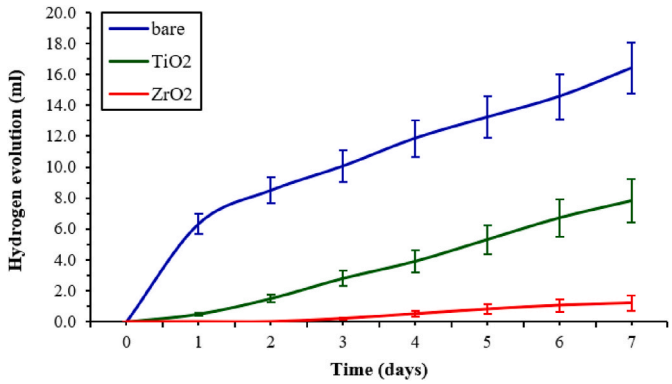

Fig. 8. Hydrogen evolution over immersion time of bare, ALD TiO_2 and ZrO_2 coated AZ31 alloy in SBF.

mode fracture features, namely ductile and brittle fracture characteristics, and both transgranular and intergranular cracks are evident, with a predominance of the former. The application of the coatings did not alter the AZ31 response mechanisms to SCC, being the fracture characterised by both a ductile and brittle zone, the latter characterised by the presence of both intergranular and transgranular cracks. However, the application of the TiO_2 coating leads to a change of the fracture appearance in the brittle zone due to the reduced embrittlement of the material, as a consequence of the reduced corrosion. In fact, while in the bare samples the transgranular fracture was predominant, the TiO_2 coated samples show intergranular cracking as the main mechanism (Fig. 11e). Finally, the application of the ZrO_2 coating leads to a failure that is predominantly ductile (Fig. 11g). This is particularly apparent in the centre of the sample, with the mixed mode fracture features close to the sample edges appearing to have experienced transgranular and intergranular cracking (Fig. 11h).

The reduced corrosion of the coated samples tested in SBF, with respect to the bare sample, is also confirmed by the tilted views of the gauge section (compare Fig. 11f and i with Fig. 11c), where deep secondary cracks and some pits can be observed in the bare samples, while no deep secondary cracks and no pits are present in the coated samples. In addition, necking can also be observed in the ZrO_2 coated samples, confirming the increased ductility (Fig. 11i).

3.7. Cytotoxicity of ALD samples

To evaluate the cytotoxicity of the different ALD coatings, we subjected L929 murine fibroblasts to treatment with extracts obtained from the bare AZ31 alloy and the coated samples, and assessed cytotoxicity through MTS assay. Fig. 12 shows the viability of L929 cells after 1, 3 and 5 days in culture, respectively, normalised against the control condition (DMEM) (Fig. 12).

4. Discussion

To be considered suitable for biomedical applications, a material must guarantee a suitable biocompatibility and an adequate resistance to Corrosion Assisted Cracking phenomena (e.g. SCC and corrosion fatigue (CF)). The low performance of Mg and its alloys in these key aspects has limited their applicability for biomedical purposes despite their great potential. Indeed, the high corrosion rate and high susceptibility to SCC have hindered the benefits achievable by an elastic modulus close to that of human bones (Peron et al., 2017; Winzer et al., 2007; Witte et al., 2005; Zberg et al., 2009). In this work, we have

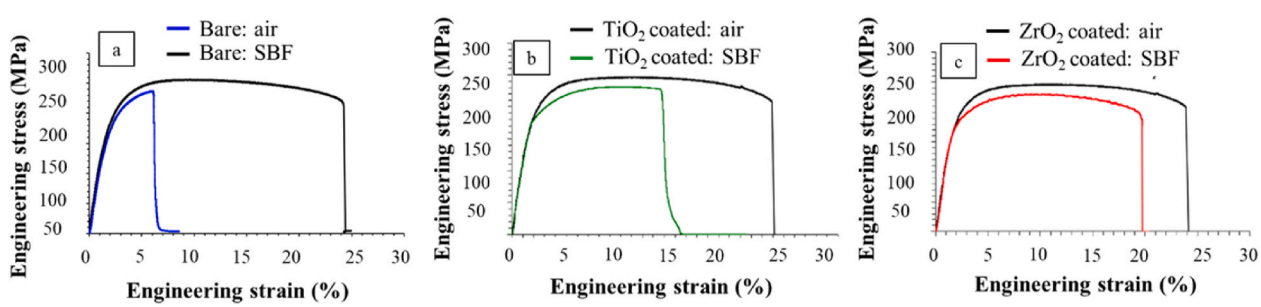

Fig. 9. Engineering stress-strain curves of bare and coated AZ31 samples tested in air and SBF.

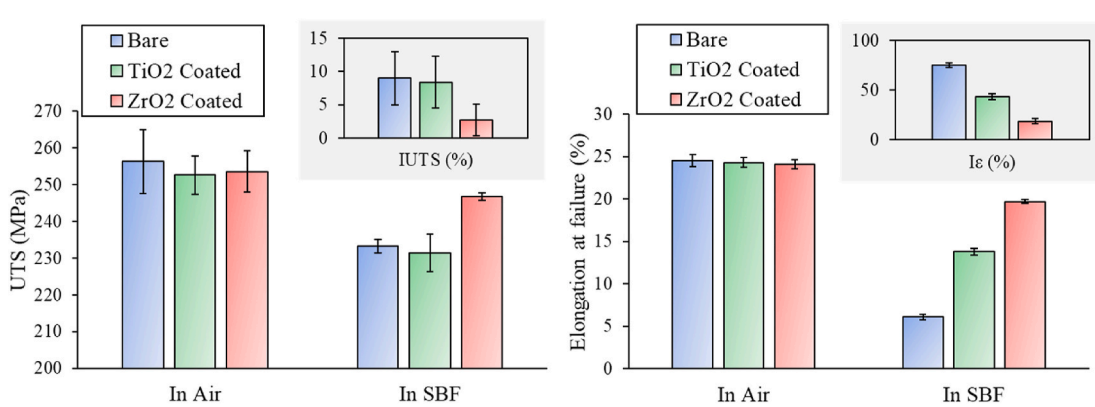

Fig. 10. Mechanical properties and SCC susceptibility indexes of bare and coated samples.

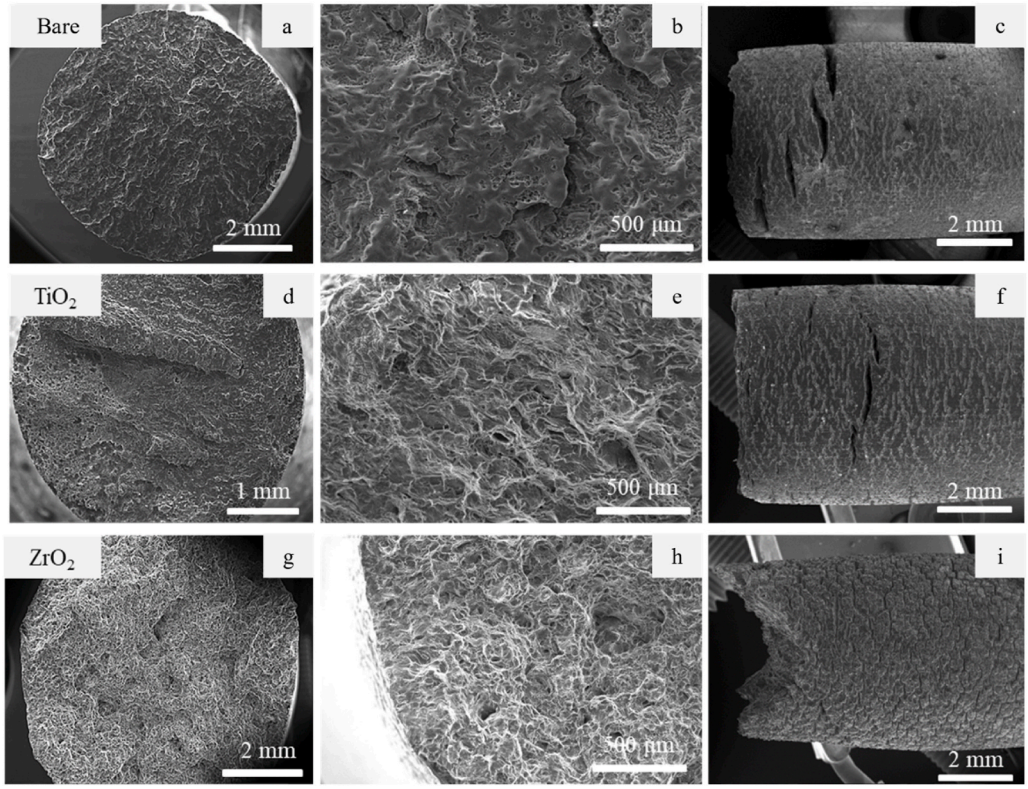

Fig. 11. SEM images of overall fracture surface (a, d, and g), magnification of a, d, and g (b, e, and h, respectively) and gauge section of the bare sample and coated AZ31 samples tested in SBF (c, f, and i).

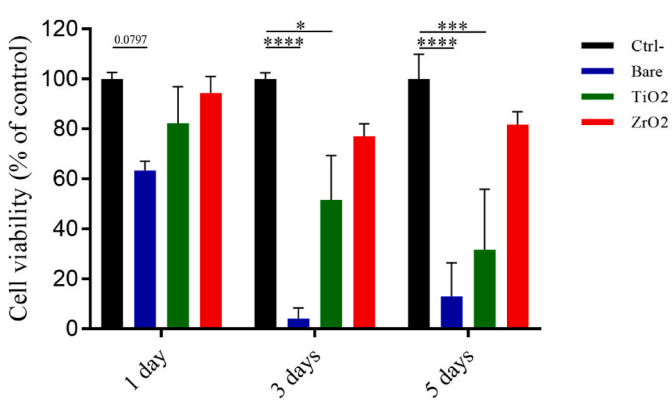

Fig. 12. Cell viability (% of control sample) of L929 fibroblasts cultured in extracts obtained from bare and coated AZ31 substrates. Cell viability was assessed after 1, 3 and 5 days in culture. Error bars represent mean ± SEM for n = 3 independent experiments, two-way ANOVA with Dunnet's multiple comparison test; $*p \leq 0.05$, $**p \leq 0.01$, $***p \leq 0.001$, $****p \leq 0.0001$).

evaluated the potentialities of ALD coatings (particularly TiO_2 and ZrO_2 coatings) to solve these issues and, for the first time, we have considered the different key aspects (i.e. corrosion resistance, SCC resistance and biocompatibility) as an indissoluble single aspect, investigating their interrelations and the causes of the different behaviours.

Considering the biocompatibility (Mg and its alloys are optimal materials for temporary implants), we decided to focus on the impact of the corrosion products on cell viability in the immediate surroundings of the implant. To do so, we evaluated the viability of L929 cells in the presence of sample extracts by using the MTS colorimetric assay. As can be observed in Fig. 12, both the ALD coatings tested increase the cell viability of the bare samples. However, not all the coatings met the demands for cellular applications (i.e. a cytotoxicity grade equal to 0 or 1, that corresponds to a cell viability ≥75% (Yang et al., 2016)). As reported in Table 6, only ZrO2 ALD coatings always showed a grade 1 cytotoxicity, while TiO2 ALD coatings met these criteria only at 1 day of culture; after that, the cell viability with TiO2 ALD coatings decreased to grade 2. Considering bare AZ31 samples, instead, they are always characterised by a too low viability to meet the demands for cellular applications, as already reported elsewhere (Kim et al., 2017).

The obtained cytotoxicity can be explained by considering the fact that a too high pH can affect the cell viability. Zhen et al., for example, reported that the proliferation of L929 cells is inhibited by a pH greater than 9 (Zhen et al., 2015). The pH behaviour can then, in turn, be linked to the corrosion behaviour: a too high corrosion rate would, in fact, increase the amount of OH- ions released from the corrosion process, thus increasing the pH. We hence evaluated the corrosion behaviour of the ALD coated and uncoated samples, in order to find a mechanistic explanation for the cytotoxicity results. We specifically adopted potentiodynamic polarisation tests and hydrogen evolution experiments and

Table 6
Cytotoxicity grade of bare and ALD coated AZ31 alloys. The cell viability values are in brackets.

Cytotoxicity Grade	0	1	2	3	4	5
Cell viability	≥100	75–99	50–74	25–49	1–24	<1
Viability at 1 day of culture		ZrO_2 (94.8%) TiO_2 (82.8%)	Bare (63.4%)			
Viability at 3 days of culture		ZrO_2 (77.6%)	TiO_2 (51.7%)		Bare (4.7%)	
Viability at 5 days of culture		ZrO_2 (81.5%)		TiO_2 (31.9%)	Bare (13.4%)	

both measurements suggest that the presence of the ALD coatings increase the corrosion resistance. The hydrogen evolution tests, for example, showed that the ALD coatings highly reduced the corrosion rate, with the ALD ZrO_2 coating being the most effective. The hydrogen evolved after 7 days from bare samples was, indeed, reduced by 93% with ALD ZrO_2 coatings, while the improvement was limited to 52% with ALD TiO_2 coatings. Similar behaviour was indicated by the potentiodynamic polarisation tests, with the ALD ZrO_2 coatings reducing the *icorr* of the bare samples by three orders of magnitude, while the ALD TiO_2 coatings by just two orders of magnitude, consistent with previous reports (Yang et al., 2017; Peron et al., 2020e, 2021; Liu et al., 2018; Marin et al., 2012b).

The improved corrosion resistance provided by the ALD coatings also had an impact on the SCC performance. An improved corrosion resistance is widely reported as decreasing the SCC susceptibility since it limits the two main causes of the SCC, i.e. the anodic dissolution and the Hydrogen Embrittlement (HE) phenomenon (Peron et al., 2017, 2020a; Jafari et al., 2015; Winzer et al., 2005). Although at different magnitudes, the SCC indexes (I_{UTS} and I_{ε}) were coherently found to be reduced by the application of the coatings: the I_{UTS} and the I_{ε} of bare samples were reduced by 7% and 42%, respectively, with TiO_2 ALD coatings, while ALD ZrO_2 coatings reduced the IUTS and the I_{ε} by 70% and 76%, respectively. Of particular interest is the drastic decrease in I_{ε}, which is much bigger than the reduction in I_{UTS}, especially for TiO2 ALD samples. The I_{ε} is, in fact, usually the most affected SCC index since the elongation to failure is more susceptible than the UTS to the embrittlement of the material caused by the HE phenomenon. The reduced embrittlement of the ALD samples and, in particular, of the ZrO_2 coated samples, was further revealed by the fractographies of the samples tested in SBF and by the tilted view of the gauge section (Fig. 11). The failure mechanism typical of the HE phenomenon (i.e. transgranular fracture) was only observable for the bare samples. The ALD TiO_2 coated samples showed predominant intergranular fracture, which is typical of anodic dissolution, while ALD ZrO_2 samples revealed a mixed brittle-ductile behaviour, where cleavage facets and dimple-like morphologies were both present (Fig. 11h). The reduced embrittlement of the ALD coated samples was also detectable by assessing the tilted views of the gauge section, with the ALD ZrO_2 coated samples even showing necking (Fig. 11i). Moreover, from the tilted views of the gauge section, it is also possible to observe that the presence of ALD coatings reduced the pitting, which is known as the main precursor for SCC crack initiation (Stampella et al., 1984; Raja and Padekar, 2013). Due to their high conformality, the ALD coatings can protect all cavities on the surface of the sample, further reducing the SCC susceptibility.

To understand the different corrosion performances, which have been shown to influence both the biological response and the SCC susceptibility, the coating integrities need to be considered together with their electrochemical properties, while, based on the results reported in Table 4, we can exclude that the coating adhesion influences the corrosion performances since both TiO_2 and ZrO_2 coatings are proved to adhere well to the substrate. Dealing with the former, defects such as pores and cracks are known to be detrimental for the corrosion resistance since they can provide a path for the fluid to access the substrate (Hamdy Makhlouf, 2015). In light of this, the lower corrosion resistance of the ALD TiO_2 coatings is not surprising since they are characterised by longer and more numerous cracks than their ALD ZrO_2 counterparts (Fig. 6). The higher defectiveness of ALD TiO_2 coatings compared to the ALD ZrO_2 counterparts is explainable considering the causes of crack formation in coated samples, which are the residual stresses arising from the difference in the thermal expansion coefficients between the coating and the substrate (Il Pyun et al., 1993; Christoph Leyens and Manfred Peters, 2003). Mg is reported to have a coefficient of thermal expansion of $27 \cdot 10^{-6}$ °C^{-1} (Yang et al., 2011), while that of TiO_2 and ZrO_2 is $7 \cdot 10^{-6}$ °C^{-1} and $11 \cdot 10^{-6}$ °C^{-1}, respectively (Hayashi et al., 2005; Hummer et al., 2007; Haggerty et al., 2014). The mismatch between the substrate and the coating is lower with ALD ZrO_2 coatings and higher with ALD TiO_2, which justifies the lower defectiveness (and hence corrosion rate) of ALD ZrO_2 coatings. The detrimental influence that defects on coatings have on the corrosion resistance is even more evident when their corrosion rates are compared with those of the bulk materials (i.e. bulk TiO_2 and ZrO_2). According to Faraday's law (Pardo et al., 2010), when exposed to SBF at 37 °C, bulk TiO_2 and ZrO_2 corrode at a rate equal to $0.37 \cdot 10^{-6}$ and $0.87 \cdot 10^{-7}$ mm/year, respectively (Lorenzetti et al., 2014; Sowa et al., 2017). However, we measured corrosion rates that were 570 and 130 times higher (i.e. $2.11 \cdot 10^{-4}$ and $1.14 \cdot 10^{-5}$ mm/year). This can be linked to the presence of defects and, due to the lower increment for ALD ZrO_2 samples, further confirmed their lower defectiveness. Dealing with the electrochemical stability, then, this further contributes to the higher corrosion resistance of ALD ZrO_2 coated samples. ZrO_2 is more electrochemically stable than TiO2 due to its higher cohesive energy (Turchanin and Agraval, 2008) (a higher cohesive energy makes a material more electrochemically stable and lowers its corrosion (Li and Li, 2006)). Moreover, the higher hydrophobicity of ALD ZrO_2 coated samples further contributes to their lower corrosion rate with respect to ALD TiO_2 (Akaltun et al., 2016): ZrO_2 has a water contact angle of around 70°, while TiO_2 is around 55° (Miyauchi et al., 2002; González-Martín et al., 1999).

In conclusion, when choosing the coating material to enable the adoption of Mg and its alloys for temporary biomedical devices, it is important to limit the corrosion rate of the Mg substrate since it has repercussions on the biological response and on the SCC susceptibility. This is particularly evident if we consider the results obtained for the cytotoxicity of ALD TiO2 coatings. TiO_2 is a widely known biocompatible material (it induces fast deposition of apatite from SBF in vitro and stimulates the adhesion and proliferation of cells (Li et al., 2013; Sun and Wang, 2008)) but, in this work, we found that its cytotoxicity grade did not meet the demands for cellular applications. The biocompatibility of TiO_2 remains undisputed when the cells are in direct contact but we have proved that biocompatibility issues may arise when TiO_2 is used as coating material for biodegradable materials like Mg and its alloys and it does not appear to be effective in reducing the corrosion rate of the substrate. This leads to the formation of an environment that is toxic for the cells. Therefore, to correctly choose the coating material for biodegradable Mg alloys, the corrosion resistance has to be tuned correctly and, to do so, it is essential to focus on its cohesive energy, wettability and thermal expansion coefficient. Only in this way would it be possible to provide an effective reduction of the corrosion rate of the Mg substrate, guaranteeing adequate performances in terms of biological response and SCC susceptibility. However, it is worth mentioning that a coating that does meet these requirements can still be considered not suitable for biodegradable Mg-based implants. CF is considered to be among the major concerns in biomedical applications (it is reported to be one of the most numerous causes of implant failures (Antunes and de Oliveira, 2012)). For this reason, how the coating behaves with respect to CF needs to be investigated, especially in light of the fact that small cracks on the coating could initiate fatigue failure. Similarly, a comprehensive evaluation of the biocompatibility of the different coatings, assessing cell morphology and adhesion behaviour, both in vitro and in vivo, is essential prior to definitely introducing these alloys into routine clinical practice.

5. Conclusions

In this study, the effect of two types of coating (TiO_2 and ZrO_2) deposited through ALD technique, on the corrosion performances and in vitro degradation of the AZ31 Mg alloy for biomedical applications, was assessed. First, the coatings were realised and characterised, in terms of chemical composition, coating thickness and number of defects. Then, the coated samples were evaluated from a corrosion point of view, by means of potentiodynamic polarisation tests, hydrogen evolution curves and SSRTs, at a strain rate of $3.5 \cdot 10^{-6}$ s^{-1} in SBF at 37 °C. The fracture surfaces after SSRT were analysed using SEM to determine corrosion

phenomena. Finally, cytotoxicity was assessed via the MTS cell proliferation assay in L929 murine fibroblasts.

The main findings can be summarised as follows:

- Spectroscopic ellipsometry measurements show that the coating thickness of TiO_2 and ZrO_2 are comparable. Nevertheless, both the crack density and the average crack length were significantly reduced in the ZrO_2 coating as compared to the TiO_2 counterpart.
- Adhesion tests proved that both coating are characterized by strong adhesion, being higher with the respect of the one of the glues used for the investigation;
- ALD coatings are effective in increasing corrosion resistance of magnesium alloys; specifically, i_{corr} was reduced by two orders of magnitude for TiO_2 and three orders of magnitude for ZrO_2 compared to the base alloy. In a similar way, the amount of hydrogen formed after 7 days was reduced by almost 52% for TiO_2 and 93% for ZrO_2 compared to the base alloy.
- ALD coatings are effective in reducing the SCC susceptibility: specifically, I_ε was reduced by 42% for TiO_2 and 76% for ZrO_2 with respect to the base alloy. Similarly, I_{UTS} was reduced by 7% for TiO_2 and 70% for ZrO_2 compared to the base alloy, respectively.
- ALD coatings considerably improve the cell viability compared to the bare sample. Nevertheless, while ZrO_2 ALD coatings showed Grade 1 cytotoxicity even after 5 days, TiO_2 ALD samples decreased from Grade 1 to 2 after 48 h.
- The better corrosion performances of ZrO_2 can be attributed to its lower density of defects, its higher electrochemical stability and hydrophobicity as compared to its TiO_2 counterpart.

Based on these results, ZrO_2 ALD coatings seem to be an effective solution to finally allow the use of Mg and its alloys as materials for temporary devices in load bearing applications. However, before giving the go-ahead for their use in such applications, a deep investigation on how these coatings behave when subjected to CF needs to be carried out, together with a comprehensive assessment of their biocompatibility both in vitro and in vivo.

CRediT authorship contribution statement

M. Peron: Conceptualization, Data curation, Methodology, Investigation, Writing – original draft. **R. Bertolini:** Visualization, Writing – original draft. **S. Cogo:** Data curation, Investigation, Formal analysis, Writing – original draft.

Declaration of competing interest

The authors declare that they have no known competing financial interests or personal relationships that could have appeared to influence the work reported in this paper.

References

Akaltun, Y., Aslan, M., Yetim, T., Çayir, T., Çelik, A., 2016. The effect of wettability on corrosion resistance of oxide films produced by SILAR method on magnesium, aluminum and copper substrates. Surf. Coating. Technol. 292, 121–131. https://doi.org/10.1016/j.surfcoat.2016.03.011.

Antunes, R.A., de Oliveira, M.C.L., 2012. Corrosion fatigue of biomedical metallic alloys: mechanisms and mitigation. Acta Biomater. 8, 937–962. https://doi.org/10.1016/j.actbio.2011.09.012.

ASTM G5 - 14 standard reference test method for making potentiodynamic anodic polarization measurements, (n.d.). https://compass.astm.org/Standards/HISTORICAL/G5-14.htm (accessed December 3, 2019).

ASTM International, ASTM-E466-96. Standard practice for slow strain rate testing to evaluate the susceptibility of metallic materials to environmentally assisted cracking, (n.d.). https://doi.org/10.1520/G0129-00R13.

Bauer, T.W., Schils, J., 1999. The pathology of total joint arthroplasty.II. Mechanisms of implant failure. Skeletal Radiol. 28, 483–497 accessed March 31, 2017. http://www.ncbi.nlm.nih.gov/pubmed/10525792.

Choudhary, L., Singh Raman, R.K., Hofstetter, J., Uggowitzer, P.J., 2014. In-vitro characterization of stress corrosion cracking of aluminium-free magnesium alloys for temporary bio-implant applications. Mater. Sci. Eng. C 42, 629–636. https://doi.org/10.1016/J.MSEC.2014.06.018.

Christoph Leyens, C., Manfred Peters, M., John Wiley & Sons, Wiley InterScience (Online service), 2003. In: Titanium and Titanium Alloys: Fundamentals and Applications. Wiley-VCH.

Curioni, M., 2014. The behaviour of magnesium during free corrosion and potentiodynamic polarization investigated by real-time hydrogen measurement and optical imaging. Electrochim. Acta 120, 284–292. https://doi.org/10.1016/J.ELECTACTA.2013.12.109.

Esmaily, M., Svensson, J.E., Fajardo, S., Birbilis, N., Frankel, G.S., Virtanen, S., Arrabal, R., Thomas, S., Johansson, L.G., 2017. Fundamentals and advances in magnesium alloy corrosion. Prog. Mater. Sci. 89, 92–193. https://doi.org/10.1016/J.PMATSCI.2017.04.011.

Ginebra, M.P., Traykova, T., Planell, J.A., 2006. Calcium phosphate cements as bone drug delivery systems: a review. J. Contr. Release 113, 102–110. https://doi.org/10.1016/j.jconrel.2006.04.007.

González-Martín, M.L., Labajos-Broncano, L., Jańczuk, B., Bruque, J.M., 1999. Wettability and surface free energy of zirconia ceramics and their constituents. J. Mater. Sci. 34, 5923–5926. https://doi.org/10.1023/A:1004767914895.

Haggerty, R.P., Sarin, P., Apostolov, Z.D., Driemeyer, P.E., Kriven, W.M., 2014. Thermal expansion of HfO_2 and ZrO_2. J. Am. Ceram. Soc. 97, 2213–2222. https://doi.org/10.1111/jace.12975.

Hamdy Makhlouf, A.S., 2015. Intelligent stannate-based coatings of self-healing functionality for magnesium alloys. In: Intell. Coatings Corros. Control. Elsevier Inc., pp. 537–555. https://doi.org/10.1016/B978-0-12-411467-8.00015-5

Hanawa, T., 2010. Overview of metals and applications. In: Met. Biomed. Devices. Elsevier Ltd, pp. 3–24. https://doi.org/10.1533/9781845699246.1.3.

Hänzi, A.C., Sologubenko, A.S., Uggowitzer, P.J., 2009. Design strategy for new biodegradable Mg–Y–Zn alloys for medical applications. Int. J. Mater. Res. 100, 1127–1136. https://doi.org/10.3139/146.110157.

Hayashi, H., Saitou, T., Maruyama, N., Inaba, H., Kawamura, K., Mori, M., 2005. Thermal expansion coefficient of yttria stabilized zirconia for various yttria contents. Solid State Ionics 176, 613–619. https://doi.org/10.1016/j.ssi.2004.08.021.

Huang, L., Su, K., Zheng, Y.F., Yeung, K.W.K., Liu, X.M., 2019. Construction of TiO2/silane nanofilm on AZ31 magnesium alloy for controlled degradability and enhanced biocompatibility. Rare Met. 38, 588–600. https://doi.org/10.1007/s12598-018-1187-7.

Hummer, D.R., Heaney, P.J., Post, J.E., 2007. Thermal expansion of anatase and rutile between 300 and 575 K using synchrotron powder X-ray diffraction. Powder Diffr. 22, 352–357. https://doi.org/10.1154/1.2790965.

Il Pyun, S., Yoon, Y.G., Lugscheider, E., Mathesius, R., 1993. Relationship between interfacial reaction and adhesion at PVD TiO2 film-metal (Ti or Al) interfaces. Surf. Coating. Technol. 61, 233–237. https://doi.org/10.1016/0257-8972(93)90231-C.

ISO 10993-12, 2012. Biological evaluation of medical devices – Part 12: sample preparation and reference materials, (n.d.). https://www.iso.org/standard/53468.html. (Accessed 26 December 2018) accessed.

ISO 10993-5, 2009. Biological evaluation of medical devices – Part 5: tests for in vitro cytotoxicity, (n.d.). https://www.iso.org/standard/36406.html. (Accessed 26 December 2018) accessed.

Jafari, S., Harandi, S.E., Singh Raman, R.K., 2015. A review of stress-corrosion cracking and corrosion fatigue of magnesium alloys for biodegradable implant applications. JOM (J. Occup. Med.) 67, 1143–1153. https://doi.org/10.1007/s11837-015-1366-z.

Kania, A., Szindler, M.M., Szindler, M., 2021. Structure and corrosion behavior of TiO2 thin films deposited by ALD on a biomedical magnesium alloy, 2021 Coatings 11, 70. https://doi.org/10.3390/COATINGS11010070.

Kim, J.H., Lee, S., Im, H.S., 1999. Effect of target density and its morphology on TiO2 thin films grown on Si(100) by PLD. Appl. Surf. Sci. 151, 6–16. https://doi.org/10.1016/S0169-4332(99)00269-X.

Kim, J., Mousa, H.M., Park, C.H., Kim, C.S., 2017. Enhanced corrosion resistance and biocompatibility of AZ31 Mg alloy using PCL/ZnO NPs via electrospinning. Appl. Surf. Sci. 396, 249–258. https://doi.org/10.1016/J.APSUSC.2016.10.092.

Kokubo, T., Takadama, H., 2006. How useful is SBF in predicting in vivo bone bioactivity? Biomaterials 27, 2907–2915. https://doi.org/10.1016/J.BIOMATERIALS.2006.01.017.

Li, W., Li, D.Y., 2006. Influence of surface morphology on corrosion and electronic behavior. Acta Mater. 54, 445–452. https://doi.org/10.1016/j.actamat.2005.09.017.

Li, H., Cui, Q., Feng, B., Wang, J., Lu, X., Weng, J., 2013. Antibacterial activity of TiO 2 nanotubes: influence of crystal phase, morphology and Ag deposition. Appl. Surf. Sci. 284, 179–183. https://doi.org/10.1016/j.apsusc.2013.07.076.

Liu, F., Shan, D., Song, Y., Han, E.-H., Ke, W., 2011. Corrosion behavior of the composite ceramic coating containing zirconium oxides on AM30 magnesium alloy by plasma electrolytic oxidation. Corrosion Sci. 53, 3845–3852. https://doi.org/10.1016/J.CORSCI.2011.07.037.

Liu, X., Yang, Q., Li, Z., Yuan, W., Zheng, Y., Cui, Z., Yang, X., Yeung, K.W.K., Wu, S., 2018. A combined coating strategy based on atomic layer deposition for enhancement of corrosion resistance of AZ31 magnesium alloy. Appl. Surf. Sci. 434, 1101–1111. https://doi.org/10.1016/J.APSUSC.2017.11.032.

Lorenzetti, M., Pellicer, E., Sort, J., Baró, M.D., Kovač, J., Novak, S., Kobe, S., 2014. Improvement to the corrosion resistance of Ti-based implants using hydrothermally synthesized nanostructured anatase coatings. Materials 7, 180–194. https://doi.org/10.3390/ma7010180.

Marin, E., Lanzutti, A., Guzman, L., Fedrizzi, L., 2012a. Chemical and electrochemical characterization of TiO 2/Al 2 O 3 atomic layer depositions on AZ-31 magnesium alloy. J. Coating Technol. Res. 9, 347–355. https://doi.org/10.1007/s11998-011-9372-8.

Marin, E., Lanzutti, A., Guzman, L., Fedrizzi, L., 2012b. Chemical and electrochemical characterization of TiO2/Al2O3 atomic layer depositions on AZ-31 magnesium alloy. J. Coating Technol. Res. 9, 347–355. https://doi.org/10.1007/s11998-011-9372-8.

Miyauchi, M., Kieda, N., Hishita, S., Mitsuhashi, T., Nakajima, A., Watanabe, T., Hashimoto, K., 2002. Reversible wettability control of TiO2 surface by light irradiation. Surf. Sci. 511, 401–407. https://doi.org/10.1016/S0039-6028(02)01551-0.

Nezar, S., Saoula, N., Sali, S., Faiz, M., Mekki, M., Laoufi, N.A., Tabet, N., 2017. Properties of TiO 2 thin films deposited by rf reactive magnetron sputtering on biased substrates. Appl. Surf. Sci. 395, 172–179. https://doi.org/10.1016/j.apsusc.2016.08.125.

Padekar, B.S., Singh Raman, R.K., Raja, V.S., Paul, L., 2013. Stress corrosion cracking of a recent rare-earth containing magnesium alloy, EV31A, and a common Al-containing alloy, AZ91E. Corros. Sci. 71, 1–9. https://doi.org/10.1016/J.CORSCI.2013.01.001.

Pardo, A., Feliu, S., Merino, M.C., Arrabal, R., Matykina, E., 2010. Electrochemical estimation of the corrosion rate of magnesium/aluminium alloys. Int. J. Corros. 2010 https://doi.org/10.1155/2010/953850.

Peron, M., Torgersen, J., Berto, F., 2017. Mg and its alloys for biomedical applications: exploring corrosion and its interplay with mechanical failure. Metals 7, 252. https://doi.org/10.3390/met7070252.

Peron, M., Berto, F., Torgersen, J., 2020a. Magnesium and its Alloys as Implant Materials: Corrosion, Mechanical and Biological Performances. CRC Press LLC.

Peron, M., Bertolini, R., Ghiotti, A., Torgersen, J., Bruschi, S., Berto, F., 2020b. Enhancement of stress corrosion cracking of AZ31 magnesium alloy in simulated body fluid thanks to cryogenic machining. J. Mech. Behav. Biomed. Mater. 101, 103429. https://doi.org/10.1016/J.JMBBM.2019.103429.

Peron, M., Skaret, P.C., Fabrizi, A., Varone, A., Montanari, R., Roven, H.J., Ferro, P., Berto, F., Torgersen, J., 2020c. The effect of Equal Channel Angular Pressing on the stress corrosion cracking susceptibility of AZ31 alloy in simulated body fluid. J. Mech. Behav. Biomed. Mater. 103724. https://doi.org/10.1016/j.jmbbm.2020.103724.

Peron, M., Bin Afif, A., Dadlani, A., Berto, F., Torgersen, J., 2020d. Comparing physiologically relevant corrosion performances of Mg AZ31 alloy protected by ALD and sputter coated TiO2. Surf. Coating. Technol. 125922. https://doi.org/10.1016/j.surfcoat.2020.125922.

Peron, M., Bin Afif, A., Dadlani, A.L., Berto, F., Torgersen, J., 2020e. Improving stress corrosion cracking behavior of AZ31 alloy with conformal thin titania and zirconia coatings for biomedical applications. J. Mech. Behav. Biomed. Mater. 111, 104005. https://doi.org/10.1016/j.jmbbm.2020.104005.

Peron, M., Cogo, S., Bjelland, M., Bin Afif, A., Dadlani, A., Greggio, E., Berto, F., Torgersen, J., 2021. On the evaluation of ALD TiO2, ZrO2 and HfO2 coatings on corrosion and cytotoxicity performances. J. Magnes. Alloy. https://doi.org/10.1016/j.jma.2021.03.010.

Pound, B.G., 2014. Corrosion behavior of metallic materials in biomedical applications. II. Stainless steels and Co-Cr alloys. Corrosion Rev. 32, 21–41. https://doi.org/10.1515/corrrev-2014-0008.

Raja, V.S., Padekar, B.S., 2013. Role of chlorides on pitting and hydrogen embrittlement of Mg–Mn wrought alloy. Corrosion Sci. 75, 176–183. https://doi.org/10.1016/J.CORSCI.2013.05.030.

Salahshoor, M., Guo, Y., 2012. Biodegradable orthopedic magnesium-calcium (MgCa) alloys, processing, and corrosion performance. Materials 5, 135–155. https://doi.org/10.3390/MA5010135, 2012.

Song, G., 2007. Control of biodegradation of biocompatible magnesium alloys. Corrosion Sci. 49, 1696–1701. https://doi.org/10.1016/J.CORSCI.2007.01.001.

Song, G., Atrens, A., StJohn, D., 2013. An hydrogen evolution method for the estimation of the corrosion rate of magnesium alloys. In: Magnes. Technol. 2001. John Wiley & Sons, Inc., Hoboken, NJ, USA, pp. 254–262. https://doi.org/10.1002/9781118805497.ch44.

Sowa, M., Łastówka, D., Kukharenko, A.I., Korotin, D.M., Kurmaev, E.Z., Cholakh, S.O., Simka, W., 2017. Characterisation of anodic oxide films on zirconium formed in sulphuric acid: XPS and corrosion resistance investigations. J. Solid State Electrochem. 21, 203–210. https://doi.org/10.1007/s10008-016-3369-2.

Stampella, R.S., Procter, R.P.M., Ashworth, V., 1984. Environmentally-induced cracking of magnesium. Corrosion Sci. 24, 325–341. https://doi.org/10.1016/0010-938X(84)90017-9.

Sun, T., Wang, M., 2008. Low-temperature biomimetic formation of apatite/TiO 2 composite coatings on Ti and NiTi shape memory alloy and their characterization. Appl. Surf. Sci. 255, 396–400. https://doi.org/10.1016/j.apsusc.2008.06.123.

Thirumalaikumarasamy, D., Shanmugam, K., Balasubramanian, V., 2014. Comparison of the corrosion behaviour of AZ31B magnesium alloy under immersion test and potentiodynamic polarization test in NaCl solution. J. Magnes. Alloys 2, 36–49. https://doi.org/10.1016/J.JMA.2014.01.004.

Turchanin, M.A., Agraval, P.G., 2008. Cohesive energy, properties, and formation energy of transition metal alloys. Powder Metall. Met. Ceram. 47, 26–39. https://doi.org/10.1007/s11106-008-0006-3.

Winzer, N., Atrens, A., Song, G., Ghali, E., Dietzel, W., Kainer, K.U., Hort, N., Blawert, C., 2005. A critical review of the Stress Corrosion Cracking (SCC) of magnesium alloys. Adv. Eng. Mater. 7, 659–693. https://doi.org/10.1002/adem.200500071.

Winzer, N., Atrens, A., Dietzel, W., Song, G., Kainer, K.U., 2007. Stress corrosion cracking in magnesium alloys: characterization and prevention. JOM (J. Occup. Med.) 59, 49–53. https://doi.org/10.1007/s11837-007-0104-6.

Witte, F., Kaese, V., Haferkamp, H., Switzer, E., Meyer-Lindenberg, A., Wirth, C.J., Windhagen, H., 2005. In vivo corrosion of four magnesium alloys and the associated bone response. Biomaterials 26, 3557–3563. https://doi.org/10.1016/j.biomaterials.2004.09.049.

Yang, H., Huang, L., Zh, M., 2011. Hot forming characteristics of magnesium alloy AZ31 and three-dimensional FE modeling and simulation of the hot splitting spinning process. In: Magnes. Alloy. - Des. Process. Prop. InTech. https://doi.org/10.5772/13778.

Yang, H., Xia, K., Wang, T., Niu, J., Song, Y., Xiong, Z., Zheng, K., Wei, S., Lu, W., 2016. Growth, in vitro biodegradation and cytocompatibility properties of nano-hydroxyapatite coatings on biodegradable magnesium alloys. J. Alloys Compd. 672, 366–373. https://doi.org/10.1016/J.JALLCOM.2016.02.156.

Yang, Q., Yuan, W., Liu, X., Zheng, Y., Cui, Z., Yang, X., Pan, H., Wu, S., 2017. Atomic layer deposited ZrO2 nanofilm on Mg-Sr alloy for enhanced corrosion resistance and biocompatibility. Acta Biomater. 58, 515–526. https://doi.org/10.1016/J.ACTBIO.2017.06.015.

Yu, J., Zhao, X., Du, J., Chen, W., 2000. Preparation, microstructure and photocatalytic activity of the porous TiO2 anatase coating by sol-gel processing. J. Sol. Gel Sci. Technol. 17, 163–171. https://doi.org/10.1023/A:1008703719929.

Zberg, B., Uggowitzer, P.J., Löffler, J.F., 2009. MgZnCa glasses without clinically observable hydrogen evolution for biodegradable implants. Nat. Mater. 8, 887–891. https://doi.org/10.1038/nmat2542.

Zhen, Z., Liu, X., Huang, T., Xi, T., Zheng, Y., 2015. Hemolysis and cytotoxicity mechanisms of biodegradable magnesium and its alloys. Mater. Sci. Eng. C 46, 202–206. https://doi.org/10.1016/j.msec.2014.08.038.